Quantum Electronics **30** (5) 435 – 440 (2000) ©2000 Kvantovaya Elektronika and Turpion Ltd

PACS numbers: 07.60.Ly; 42.15.Dp; 42.87.Bg
DOI: 10.1070/QE2000v030n05ABEH001737

A method for measuring the radiation wave front by using a three-wave lateral shearing interferometer

A M Nugumanov, R V Smirnov, V I Sokolov

Abstract. An analysis of and some corrections to the technique of phase distribution measurement by means of a three-wave lateral shearing interferometer are made. The technique offers high precision and a wide dynamical range; it is also rather simple and handy when applied to various fields. The device for the wave front reconstruction and the data-processing algorithm is described. The results of the model simulation of the wave front meter as well as the experimental results are presented.

1. Introduction

Wave front analysis of laser radiation, adaptive optics, testing of optical elements, and studies of the atmospheric turbulence effects in astronomy all require exact reconstruction of the radiation phase. Two approaches to this problem are well-known: the interference techniques and the Hartmann test. Recently, a new method was presented in a number of papers [1 – 3], which combines these two approaches [2, 4]. The method is based on interference of three replicas of the original wave and the use of the achromatic three-wave lateral shearing interferometer (ATWLSI) as a wave front meter (WFM).

This method, in principle, allows recovering the two-dimensional phase distribution from only one interferogram. Furthermore, it does not require temporal or spatial splitting of the beam and the use of an external source of reference radiation. The practical utilisation of this method [5, 6] revealed its high precision, good spatial resolution and a wide dynamical range, which is easily tunable on a large scale.

We have developed a mathematical model of the WFM, which includes a specific algorithm of interferogram processing. Using this model, we carried out the performance analysis of the proposed method and considered its dependence on the construction and the parameters of the WFM and the data-processing algorithm. We also performed test measurements of the laser beam wave front. Based on the results of the experiments and the simulation, necessary modifications were introduced in the device construction and the phase-reconstruction algorithm.

A M Nugumanov, R V Smirnov, V I Sokolov State Scientific Centre of the Russian Federation 'Troitsk Institute of Innovation and Fusion Research', 142092 Troitsk, Moscow region, Russia

Received 26 November 1999
Kvantovaya Elektronika **30** (5) 435 – 440 (2000)
Translated by I V Bargatin, edited by M N Sapozhnikov

2. The principle of achromatic three-wave lateral shearing interferometer

The key element of the interferometer is the wave-front replicator R (Figs 1, 2). In an ATWLSI, this may be a hexagonally packed lattice of holes, a microlens array or a three-level phase grating of a similar geometry. A radiation wave propagating through such a device is diffracted by three linear structures, turned by 120° with respect to each other. As a result, six replicas of the original wave appear, which have the same wave front structure.

The directions of the corresponding wave vectors $\boldsymbol{k}_i$ are defined by the position of the first-order diffraction maxima and make the angle $\alpha = \lambda/d$ with the optical axis z, where λ is the radiation wavelength and d is the lattice spacing. The projections of the vectors $\boldsymbol{k}_i$ on the replicator plane make angles of 120° with each other. Three of the six vectors $\boldsymbol{k}_i$ are shown in Fig. 1.

The general schematic of the device is shown in Fig. 2. The interferograms are detected with a CCD camera installed on a table that provides precise longitudinal movement of the camera for detection of interferograms in different planes. A Keplerian telescope transfers the image of the replicator R plane to the CCD matrix with reduction. Diaphragms pro-

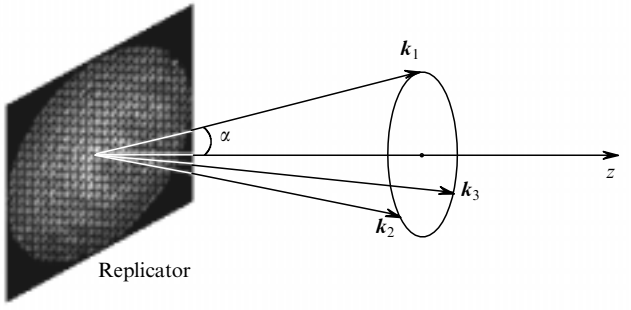

Figure 1. Schematic diagram illustrating the action of the wave front replicator.

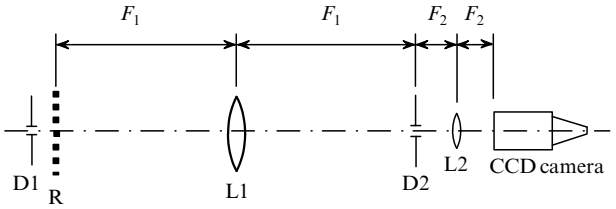

Figure 2. General schematic of the wave front meter: D1 and D2 are the diaphragms; R is the replicator; L1 and L2 are the telescope lenses.

vide the necessary alignment of the laser beam and the optical axis of the wave-front meter. Moreover, special filtering diaphragms can be installed in position D2 to select required harmonics from the Fourier spectrum of the measured radiation (see Section 4).

3. Data-processing algorithm

The proposed algorithm of phase reconstruction is based on the following intensity transport equation, which can be derived [7] from the Helmholtz equation,

$$-k\frac{\partial I(x,y;z)}{\partial z} = \nabla I(x,y;z)\nabla W(x,y;z) + I(x,y;z)\Delta W(x,y;z), \quad (1)$$

where $I(x,y;z)$ is the intensity of radiation propagating along the z axis; $W(x,y;z)$ is the radiation phase; $k = 2\pi/\lambda$ is the wave number; $\nabla = (\partial/\partial x, \partial/\partial y)$ is the gradient operator; and $\Delta = \partial^2/\partial x^2 + \partial^2/\partial y^2$ is the Laplacian.

The phase modulation induced by the periodic structure leads to the appearance of new harmonics in the radiation Fourier spectrum. Therefore, the transport equation can be effectively solved through a Fourier transformation followed by filtering of the first-order harmonics [8]. Information about the phase can be extracted from two interferograms, of which one is detected in the zero plane, which is optically conjugated to the grating plane, and the second, in the plane shifted from the zero plane by a small distance L along the z-axis. Primot et al. [1, 2] developed this approach for the case of hexagonal structures and derived the following expression for the intensity distribution in the shifted plane $I_L(\boldsymbol{x}) = I(x,y;z=L)$:

$$I_L(\boldsymbol{x}) = I(\boldsymbol{x})\left\{3g(\boldsymbol{x}) + \sum_{i,j=1,i\neq j}^{3}\left[g(\boldsymbol{x}) - \mathrm{i}L\sqrt{3}\alpha\frac{\partial W(\boldsymbol{x})}{\partial \boldsymbol{u}_{ij}}\right]\times\exp\left[\mathrm{i}k\boldsymbol{u}_{ij}\boldsymbol{x}\right]\right\}, \quad (2)$$

$$g(\boldsymbol{x}) = 1 - \frac{L}{k}\left[\Delta W(\boldsymbol{x}) + \frac{\nabla I(\boldsymbol{x})\nabla W(\boldsymbol{x})}{I(\boldsymbol{x})}\right], \quad (3)$$

where $\partial W(\boldsymbol{x})/\partial \boldsymbol{u}_{ij}$ is the derivative of the phase along the vector

$$\boldsymbol{u}_{ij} = \frac{1}{k}(\boldsymbol{k}_i - \boldsymbol{k}_j).$$

Note that the coefficient $\sqrt{3}$ is missing in Eqn (2) of Ref. [1], which leads to the corresponding proportional error in phase calculation.

Primot [1] also presented an algorithm for the reconstruction of the phase $W(x,y)$ from only one interferogram $I_L(\boldsymbol{x})$, which is an appealing option since only one measurement is needed in that case. In our model simulations, we used two algorithms to calculate the phase derivatives. The first algorithm is equivalent to the one used in Ref. [1]: only one distribution $I_L(\boldsymbol{x})$ is analysed through a Fourier transformation and recentering of the filtered harmonics according to the value of the replicator frequency. In the second algorithm, two distributions are used: the shifted-plane distribution $I_L(\boldsymbol{x})$ and the zero-plane distribution $I_0(\boldsymbol{x}) = I(x,y;z=0)$. Recentering of the Fourier harmonics is not required in this case. The second variant is, in fact, similar to the algorithm used in Ref. [8] after a corresponding adaptation for the ATWLSI; however, no intensity derivative $\partial I(\boldsymbol{r})/\partial z$ is calculated in our case.

Our calculations show that, in the first variant, the recentering operation introduces a significant error, and the accuracy, comparable to that of the second variant, can be obtained only under special conditions. Namely, the spatial frequencies of the replicator and the registering device must be multiple with respect to each other, which is rather difficult to realise in experiment. For this reason, we decided in favour of the second variant, although it requires two measurements instead of one and accounting for the intensity variation in the two measurements.

We briefly describe this algorithm below. At the first stage, a two-dimensional Fourier transformation of the intensity distribution $I_L(\boldsymbol{x})$ is performed:

$$H(f_x,f_y) = \mathfrak{F}\{I_L(x,y)\} = 3\mathfrak{F}\{I(\boldsymbol{x})g(\boldsymbol{x})\} + \sum_{i,j=1,i\neq j}^{3}\mathfrak{F}\left\{I(\boldsymbol{x})\left[g(\boldsymbol{x}) - \mathrm{i}L\sqrt{3}\alpha\frac{\partial W(\boldsymbol{x})}{\partial \boldsymbol{u}_{ij}}\right]\exp\left[\mathrm{i}k\boldsymbol{u}_{ij}\boldsymbol{x}\right]\right\}, \quad (4)$$

where $\mathfrak{F}$ is the Fourier transformation operator. One can see from Eqn (4) that the Fourier transformation of the interferogram consists of seven major components: a zero harmonic and six first-order harmonics, which correspond to the vertexes of a regular hexagon (Fig. 3). The frequencies of these harmonics are defined by the replicator lattice spacing. If the radiation intensity at the replicator aperture changes smoothly and variations in the radiation phase are slow with respect to its modulation (which is determined by the grating spacing), the harmonics are well resolved and can be successively isolated for subsequent processing.

At the second stage, the Fourier spectrum is filtered to isolate three first-order harmonics, which are located at the vertexes of an equilateral triangle. These harmonics correspond to the three vectors $\boldsymbol{u}_{ij}\,(i,j = 1,2,3, i<j)$ in the real plane. The three filtering functions $T_{ij}(f_x,f_y)$ that isolate these harmonics are nonzero in the vicinities of the centres of the corresponding harmonics:

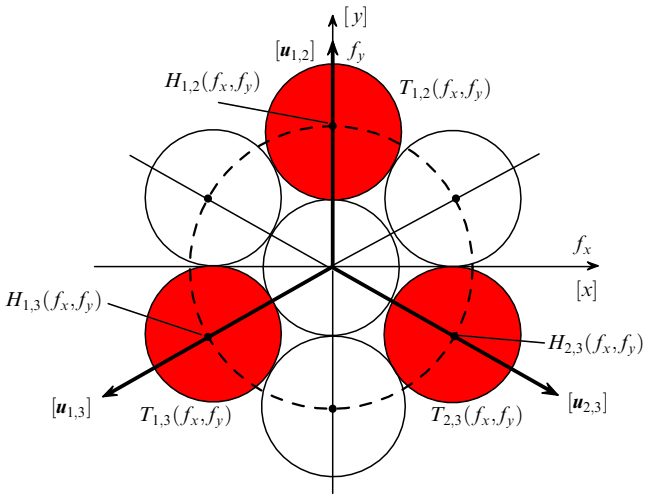

Figure 3. Geometry of the real plane and the Fourier plane: x, y are the coordinates in the real plane; f_x, f_y are the coordinates in the Fourier plane; $H_{ij}(f_x,f_y)$ are the centres of the selected harmonics; and $\boldsymbol{u}_{ij}$ are the vectors corresponding to these harmonics. The filtering functions $T_{ij}(f_x,f_y)$ are nonzero in the grey areas.

$$h_{ij}(f_x, f_y) = T_{ij}(f_x, f_y)H(f_x, f_y)$$
$$= \mathfrak{F}\left\{ I(\boldsymbol{x})\left[g(\boldsymbol{x}) - \mathrm{i}L\sqrt{3}\alpha \frac{\partial W(\boldsymbol{x})}{\partial \boldsymbol{u}_{ij}} \right] \exp\left[\mathrm{i}k\boldsymbol{u}_{ij}\boldsymbol{x}\right] \right\},$$
$$i, j = 1, 2, 3, \quad i < j. \tag{5}$$

Fig. 3 shows the corresponding geometry in the real and the Fourier planes. The symbols referring to the real plane are enclosed in square brackets.

At the third stage, we find the inverse Fourier transformation of each of the three isolated harmonics,

$$Z_{ij}^{L}(x, y) = \mathfrak{F}^{-1}[h_{ij}(f_x, f_y)]$$
$$= I(\boldsymbol{x})\left[g(\boldsymbol{x}) - \mathrm{i}L\sqrt{3}\alpha \frac{\partial W(\boldsymbol{x})}{\partial \boldsymbol{u}_{ij}} \right] \exp\left[\mathrm{i}k\boldsymbol{u}_{ij}\boldsymbol{x}\right]. \tag{6}$$

Then, the interferogram $I_0(x)$ is processed through the same sequence of operations:

$$Z_{ij}^{0}(x, y) = \mathfrak{F}^{-1}\left\{ T_{ij}(f_x, f_y)\mathfrak{F}[I_0(x, y)] \right\}$$
$$= I(\boldsymbol{x}) \exp\left[\mathrm{i}k\boldsymbol{u}_{ij}\boldsymbol{x}\right], \quad i, j = 1, 2, 3, \quad i < j. \tag{7}$$

Using Eqns (6) and (7), we find the derivatives of phase with respect to the following three directions

$$\frac{\partial W(\boldsymbol{x})}{\partial \boldsymbol{u}_{ij}} = \frac{1}{L\sqrt{3}\alpha} \operatorname{Im} \frac{Z_{ij}^{L}(x, y)}{Z_{ij}^{0}(x, y)} \tag{8}$$

and finally calculate the orthogonal directional derivatives $\partial W/\partial x$, $\partial W/\partial y$.

At the fourth stage, we recover the phase distribution

$$W(x, y) = \mathfrak{F}^{-1}\left[\frac{f_x h_x(f_x, f_y) + f_y h_y(f_x, f_y)}{f_x^2 + f_y^2} \right], \tag{9}$$

where

$$h_x(f_x, f_y) = \mathfrak{F}\frac{\partial W}{\partial x}; \quad h_y(f_x, f_y) = \mathfrak{F}\frac{\partial W}{\partial y}.$$

Formula (9) is based on the fact that the differentiation $\partial/\partial x$, $\partial/\partial y$ of a function in the real space is equivalent to multiplication by f_x and f_y, respectively, in the Fourier space [9].

4. Simulation of the WFM

To analyse the proposed method, we developed a mathematical model of the WFM, which includes the above algorithm and simulates the whole process of the phase measurement. The phase distribution $W(\boldsymbol{x})$, intensity distribution $I_0(x)$ and the wavelength λ are assumed to be specified. The distribution $I_0(\boldsymbol{x})$ here can be either calculated from the parameters of the grating and the radiation (Fig. 4a) or measured experimentally with a WFM (see Fig. 7a below). In the case of a microlens array or a phase grating, one must consider the corresponding phase modulation.

We used the spectral method for solving the parabolic equations [10] to simulate the wave propagation at the distance L after the replicator. The spectral method exploits shifts of the radiation spectrum in the Fourier space. This allowed simultaneous simulation of the arrangement of different diaphragms in the WFM telescope focal plane by superposing the corresponding filter functions over the radiation Fourier spectrum. The resulting distribution $I_L(\boldsymbol{x})$, together with the distribution $I_0(\boldsymbol{x})$, are used as the entry data in the algorithm presented in Section 3. Finally, a comparison between the calculated and the given phase distributions yielded the accuracy of the reconstruction.

We studied the dependence of the accuracy of the phase reconstruction on the radiation parameters, the displacement L, the spacing and the type of the replicator (a lattice, a microlens array, or a three-level phase grating). We consid-

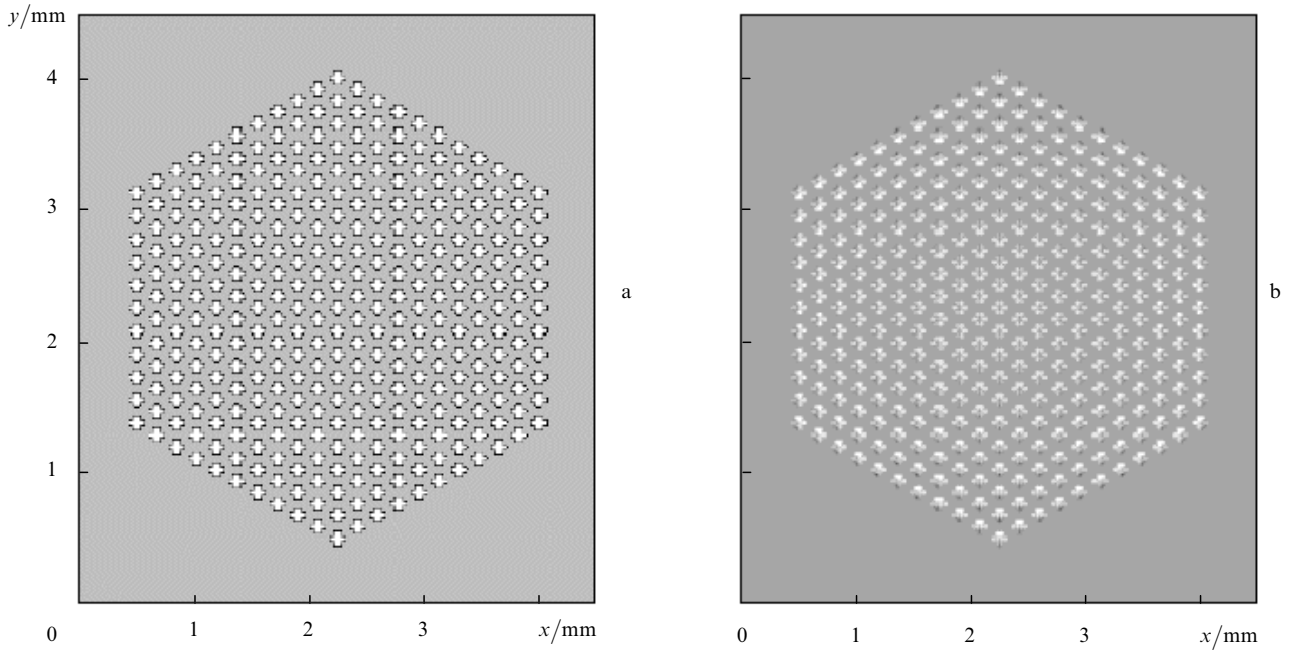

Figure 4. The computer-generated distribution of the radiation intensity at the replicator plane (a) and the difference between the distributions in the zero plane and the shifted plane (b) for the case of a spherical wave front with the radius $R = 90$ mm and the displacement $L = 1$ mm.

ered the square and hexagonal packing of round, square, and hexagonal cells. Fig. 4 shows the uniform radiation intensity dis-tribution $I_0(\boldsymbol{x})$ and the difference between the distributions in the zero plane and the shifted plain for the case of a hexagonally packed array of hexagonal holes.

The results of the calculations showed that, everything else being equal, the square packing leads to greater errors in the phase reconstruction than the hexagonal one. On the other hand, the cell shape only affects the intensity efficiency of the replicator and does not affect the measurement accuracy. For some values of the radiation and meter parameters, we determined the permissible range of the shift distance L, which is bounded below by the resolution of the CCD camera, and above by the diffraction from the grating. We found that, due to smaller influence of the diffraction, the microlens array permits a greater range of values of the displacement L. The corresponding increase of the permissible range of the wave front curvature is very important for studies of diffraction-quality wave fronts. The considered model also allows the analysis of the dependence of the measurement accuracy on the noise characteristics of the CCD camera, its instrumental function and the matrix dimensions.

Fig. 5 shows the results of a model reconstruction of the phase for $\lambda = 1.064$ μm and the displacement $L = 1$ mm. We used the WFM to measure the distribution $I_0(\boldsymbol{x})$ (see Fig. 7a below). The measured distribution was then superimposed on a spherical wave front with the radius $R = 614$ cm, which corresponded to a phase shift of 9λ in the aperture with a diameter of 22 mm. We successfully recovered the correct spherical shape of the wave front and observed a good agreement between the original (dashed line) and the reconstructed (solid line) radii of curvature (Fig. 5). The root-mean-square deviation of the estimated phase from the actual one was 0.13λ; the maximum deviation amounted to 0.38λ.

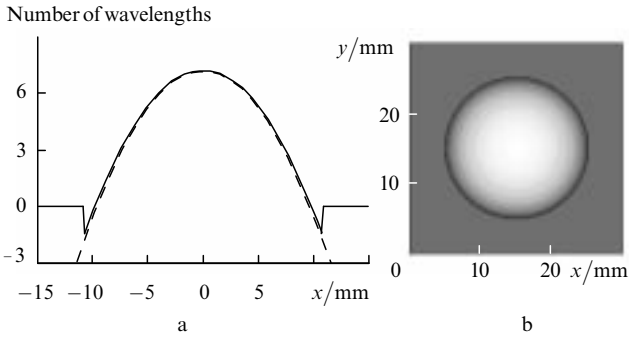

Figure 5. Phase reconstruction from the simulated measurement data. (a) The profiles of the original (dashed curve) and the reconstructed (solid curve) wave front; (b) the surface of the wave front.

We also simulated the WFM performance with various diaphragms placed in the focal plane of the telescope. In fact, without a diaphragm, the considered method is equivalent to a Hartmann test. The introduction of a diaphragm leads to a cut-off of the higher harmonics in the radiation Fourier spectrum, thereby simplifying the Fourier spectrum of the interferogram and its processing. It is natural to keep only the first-order harmonics, which are used in the subsequent processing. Note that the the choice of the diaphragm size requires some accuracy since a partial cut-off of the first-order harmonics or a partial transmission of the second-order harmonics result in significant errors in the phase measurement.

It is interesting to consider the trefoil mask, which transmits three of the six first-order harmonics (Fig. 6). In that case, the considered WFM becomes an ATWLSI [2]. The installation of such a mask leads to the most accurate analysis

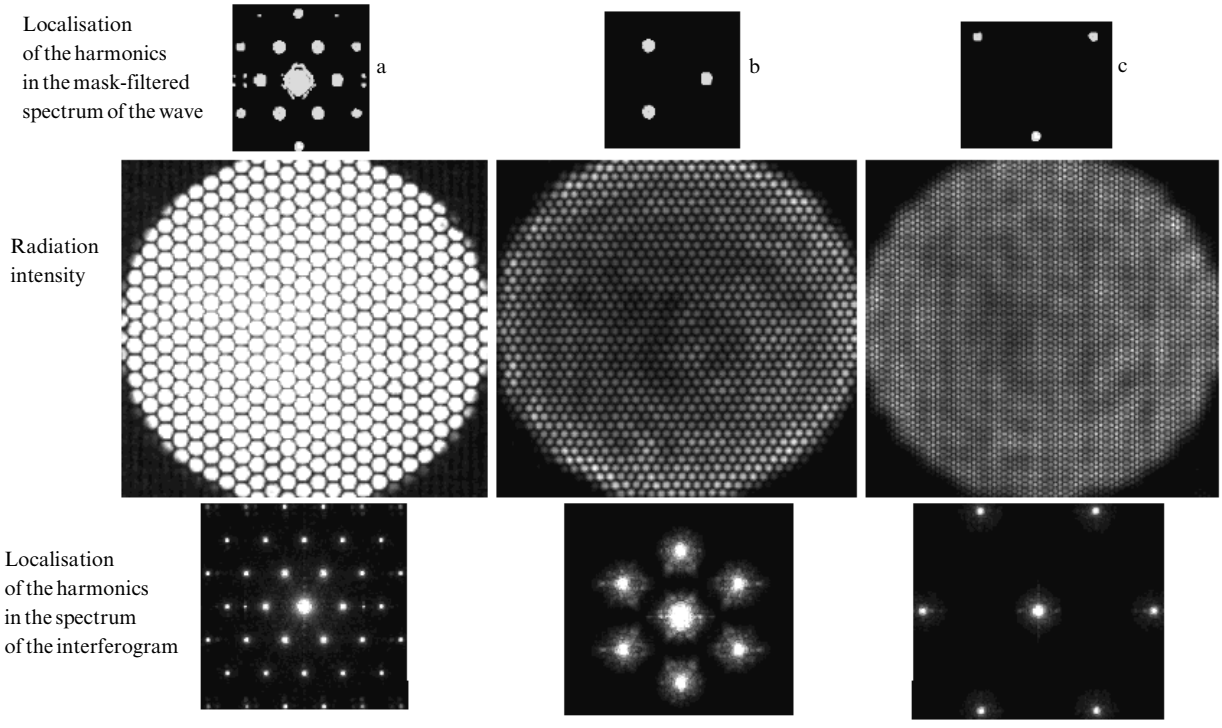

Figure 6. Spectra and interferograms obtained without mask (a) and with the first-order trefoil mask (b) and the second-order trefoil mask (c).

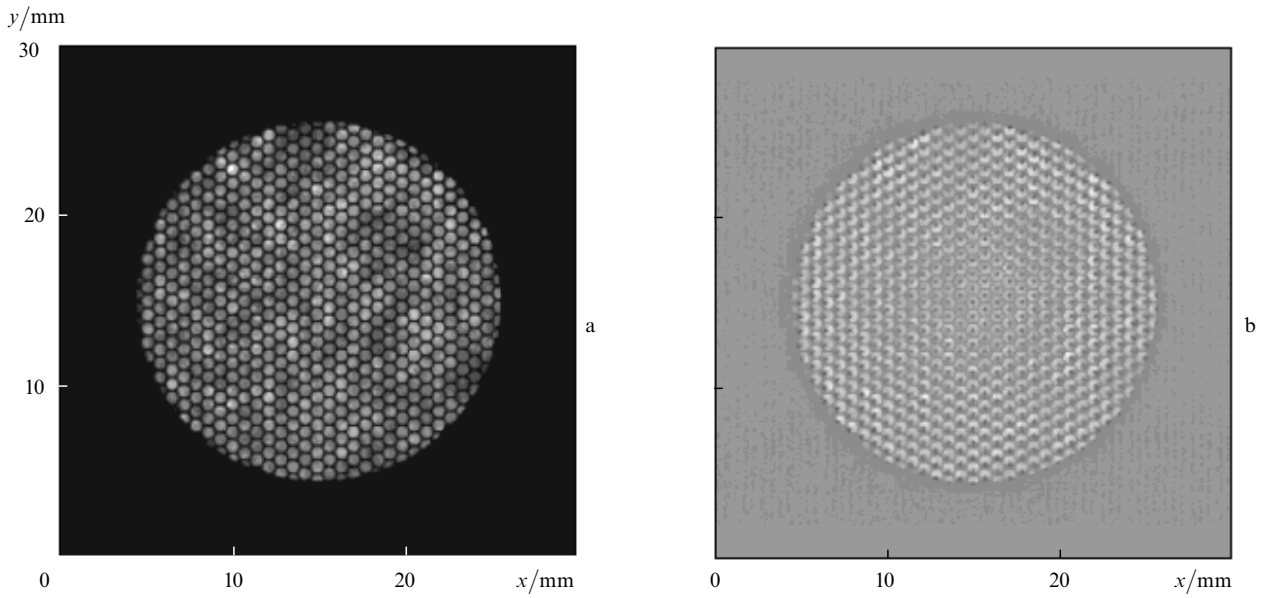

Figure 7. Experimentally measured intensity distribution in the replicator plane (a) and the difference between the intensity distributions in the zero plane and the shifted plane (b) for a spherical wave front with $R = 614$ cm and the displacement $L = 1$ mm.

of quasiplane wave fronts [5, 6] due to suppression of diffraction by the grating, which allows one to further increase the displacement L without blurring the image. Note that this mask changes the spatial frequency and the orientation of the interferogram due to filtration-induced changes in the spectrum.

Fig. 6a shows the arrangement of the spectral harmonics of the radiation transmitted through the grating, as well as the intensity distribution and the arrangement of the harmonics in the intensity spectrum. The spectra and interferograms for two different masks separating three first-order harmonics and three second-order harmonics are shown in Figs 6b and 6c, respectively. In the case shown in Fig. 6b, the orientation of the interferogram is orthogonal to the original one, and the spacing multiplier equals $\beta = \sqrt{3}$ according to the corresponding changes in the orientation and the spacing of harmonics of the spectrum.

Note that the obtained value $\beta = \sqrt{3}$ differs from those derived in Ref. [2] ($\beta = 2$) and Ref. [6] ($\beta = 1.5$). This is important because upon installation of the mask the denominator in the right-hand side of Eqn (8) should be multiplied by β. In Fig. 6c, the interferogram orientation remains unchanged and $\beta = 3$. The difficulties related to fabrication and installation of such a mask can be mitigated by increasing the replicator frequency, which leads to a corresponding increase in the spacing between harmonics in the Fourier spectrum. However, this requires the use of a CCD camera with a higher spatial resolution.

5. Experimental wave-front measurements

Based on the simulation results, we fabricated a variant of the WFM described in Section 3. A hexagonally packed grating of hexagonal cells served as the replicator. The spacing of the grating was 864 μm; the hole size was 650 μm; and the aperture diameter was 22 mm. Two telescope lenses with focal distances of $F_1 = 220$ mm and $F_2 = 36$ mm provided a six-fold reduction of the image, which was detected by a Spiricon LBA-400PC unit equipped with a COHU-6410 camera. The elements of the WFM were installed in optical mounts on a single platform. This allowed us to align the WFM on a table equipped with a radiation source of the necessary wavelength, and then transfer the device as a whole into the general optical system. Fig. 7 shows the radiation intensity distribution measured with the WFM.

We used a Laser Compact LKS-DTL-222 laser as the radiation source $\lambda \sim 1.064$ μm. The laser beam was focused with a lens on the diaphragm, which served as a point source

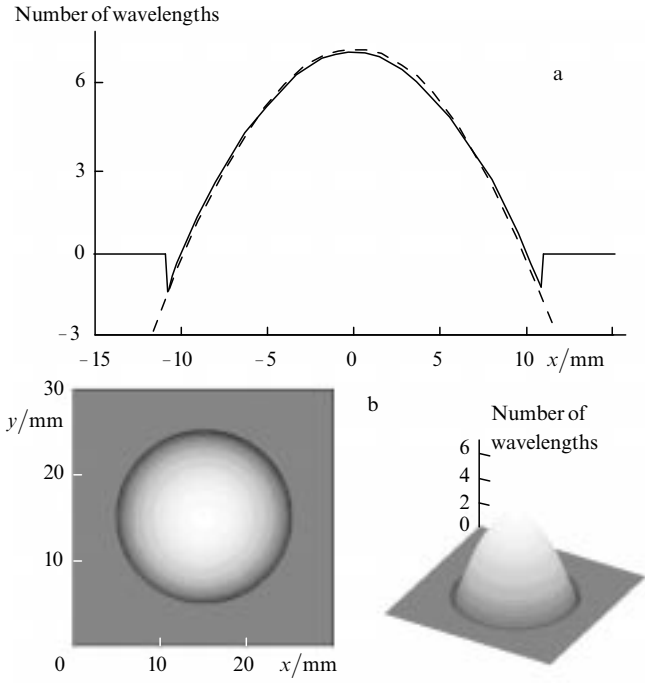

Figure 8. The reconstructed (dashed curve) and the measured (solid curve) profiles of the laser beam wave front (a); the surface of the wave front (b).

of spherical waves with a radius of 614 cm. The intensity distributions were measured using the displacement $L = 1$ mm. Fig. 8a shows a spherical profile with a radius of 614 cm (dashed line) and the reconstructed wave front profile (solid line). One can see that the theoretical curve and the reconstructed phase curve agree well for virtually all points of the aperture. The root-mean-square deviation σ of the reconstructed wave front from the original one was 0.15λ; the maximum deviation amounted to 0.56λ. The reconstructed wave front surface is shown in Fig. 8b.

6. Conclusions

The developed mathematical model of the wave-front measurement permits the analysis of different variants of the WFM design and the data-processing algorithm. The performed simulations enabled us to introduce necessary corrections into the data-processing algorithm. Namely, we chose in favour of the wave-front reconstruction algorithm based on two intensity distributions: the zero-plane one and the shifted-plane one; we also corrected a coefficient in the phase calculation formula (2) as well as the spacing multiplier β for the WFM filtering diaphragms. Based on the result of the simulations, we manufactured a WFM, which was used for experimental measurements of the phase. The results of the simulation and the experiments demonstrated the potential of the proposed technique for measurement of the phase of the laser radiation.

Acknowledgements. The authors thank V G Kuznetsov, A D Rozhkov, R G Bikmatov, and D M Kulakov for help in preparation and realisation of the experiments. We are also grateful to J Primot, J-C Chanteloup, and V M Chernyak for useful discussions of different aspects of this measurement technique. This work was supported by the International Centre of Science and Technology, project no. 591.

References

1. Primot J Appl. Opt. **32** 6242 (1993)
2. Primot J, Sogno L J. Opt. Soc. Am. **12** 2679 (1995)
3. Primot J, Sogno L, Fracasso B, Heggarty K Opt. Eng. **36** 901 (1997)
4. Roddier F Appl. Opt. **29** 1402 (1990)
5. Chanteloup J-C, Baldis H, Migus A, Mourou G, Loiseaux B, Huignard J-P Opt. Lett. **23** 475 (1998)
6. Chanteloup J-C, Druon F, Nantel M, Maksimchuk A, Mourou G Opt. Lett. **23** 621 (1998)
7. Teague M R J. Opt. Soc. Am. **72** 1199 (1982)
8. Ichikawa K, Lohmann A W, Takeda M Appl. Opt. **27** 3433 (1988)
9. Roddier F, Roddier C Appl. Opt. **30** 1325 (1991)
10. Elkin N N, Napartovich A P Prikladnaya Optika Lazerov [Applied Laser Optics] (Moscow: TsNIIatominform, 1988)